Int. J. Heat Mass Transfer. Vol. 36. No. 3. pp. 713–723. 1993
Printed in Great Britain

0017-9310/93 $6.00+0.00

The binary alloy problem in an expanding domain: the microsegregation problem

SURESH SUNDARRAJ and V. R. VOLLER
Department of Civil and Mineral Engineering, University of Minnesota, Minneapolis, MN 55455, U.S.A.

(*Received* 6 *August* 1991 *and in final form* 17 *February* 1992)

Abstract—A general numerical model of microsegregation and solidification in coarsening (i.e. expanding) secondary dendrite arms is developed. General governing equations representing the diffusive heat and mass transfer in an expanding domain are presented. The governing equations are transformed using enthalpy type variables (to deal with the moving solidification interface $s(t)$) and a Landau transformation (to deal with the expanding domain $X(t)$). This transformation allows for a fixed grid 'node jumping' numerical solution. The resulting solutions compare favorably with existing experiments and require only a fraction of the CPU time of alternative approaches.

1. INTRODUCTION

SOLIDIFICATION phenomena occur across a wide range of length scales, a feature reflected in the modeling of solidification systems. In general, models of solidification systems can be placed into one of three classes.

Macro. Models at the macroscopic level emphasize the heat and mass transfer mechanisms and are designed to predict the large scale features of a solidification process, e.g. solidification time, species transport, etc. In such models, however, it is important to recognize that macroscopic solidification events are often driven by the microscopic phenomena. Recent macro solidification models [1–4] attempt to represent appropriate microscopic behavior with suitable constitutive relationships.

Micro–macro. In 'micro–macro' modeling [5–7] the aim is the prediction of microstructure using microscopic growth and nucleation models. These models require a cooling rate as an input. Appropriate cooling rates are predicted from a macroscopic heat transfer model.

Micro. Many solidification models are purely microscopic models, on the scale of the dendrite arms in the solid/liquid mushy zone, in which macroscopic features are neglected [8–15].

The emphasis in this paper is on the development of a microscopic solidification model. Such models (1) can provide important insight (and often quantitative predictions) of microscopic behavior and (2) can be used as the micro component in a micro–macro model or as the basis of a constitutive equation in a macro model. Recent micro solidification models appearing in the literature are directed at the analysis of microsegregation (micro-compositional variation) in conjunction with coarsening of the secondary dendritic arms [12–15]. These models predict the microstructure (final secondary arm spacing) and the microsegregation (characterized by the amount of eutectic formed). The development of a microsegregation arm coarsening model is the aim of this paper.

2. THE BINARY ALLOY PROBLEM IN AN EXPANDING DOMAIN

2.1. *The microsegregation problem*

A feature in the solidification of binary alloys is the formation of a solid + liquid mushy zone. The solid crystals in the mushy zone commonly have a columnar morphology, consisting of primary and secondary dendrites [16], see Fig. 1. The length scale in this morphology is characterized by the secondary dendrite arm spacing typically of the order of tens of microns. As this binary alloy solidifies the rejected solutal phase diffuses within the dendrite spacings; a process referred to as microsegregation. The nature of this microscopic mass diffusion determines the local liquid fraction and ultimately the macroscopic behavior of the solidification. Many existing macroscopic solidification models [7] employ liquid fraction temperature relationships based on simplified limiting treatments of microsegregation, principally the Scheil and lever rules [16]. An objective of microsegregation modeling is to arrive at a more comprehensive treatment of the coupled heat and mass transfer during the local solidification between secondary dendrite arms. This process can be described on considering a one-dimensional plane front solidification controlled by coupled heat and mass diffusion. In this respect the problem can be readily identified as a variation of the well documented binary alloy problem [17–22]. The key ingredients in the microsegregation problem, which separates it from other binary alloy problems are:

NOMENCLATURE

c	specific heat
C	composition
C_0	nominal composition of the alloy
D	mixture mass diffusion coefficient
f	local liquid mass fraction
F_s	solidus curve
F_l	liquid curve
g	local liquid volume fraction
H	enthalpy
ΔH	latent heat of fusion
k_0	partition coefficient
K	mixture thermal conductivity
m_l	representative liquidus slope
q	prescribed heat flux
$s(t)$	position of the phase front in the real domain
S^H	convective source term in the heat transfer equation
S^C	convective source term in the mass transfer equation
t	time
t_s	final solidification time
Δt	time step
T	temperature
T_f	fusion temperature
T_i	initial temperature
T_{liq}	liquidus temperature
T_{sol}	solidus temperature
$T_0(t)$	time dependent temperature at $x = 0$
U	rate of interface movement
V	chemical activity
x	coordinate in the real domain
$X(t)$	length of the expanding real domain
Y	solvent in a Y–Z binary alloy
Z	solute in a Y–Z binary alloy.

Greek symbols

α	thermal diffusivity
Γ	Gibbs–Thomson coefficient
γ	interfacial surface energy
λ_2	secondary dendritic arm spacing
ξ	coordinate in the transformed domain
$\Delta\xi$	space step in the transformed domain
ρ	mass density of the alloy.

Subscripts

Al	aluminum
Cu	copper
eut	eutectic
e, w	location of control volume interface
l	liquid
P, E, W	location of node point
s	solid.

Superscript

old	old value.

(1) The size of the domain is at the microscopic level, i.e. half the secondary arm spacings, $X(t)$, Fig. 1(b). In other binary alloy problems [17–22] no explicit length scale is given.

(2) The secondary dendrite arm spacings expand as the solidification proceeds. This phenomena of 'coarsening' occurs by 'melting back' or breaking off ('necking') [23] of some of the arms. Thus the dendrite arm spacing and likewise the microsegregation solution domain $X(t)$ is not fixed but changes with time, Fig. 1(c).

2.2. *The microsegregation model*

Consider a binary alloy (e.g. aluminum–copper) contained in the expanding domain $0 < x < X(t)$, Fig. 1(b). Initially the alloy is in the liquid state with a uniform composition C_0 (wt % of Z in Y) and a uniform temperature $T_i \geqslant T_{liq}$ (the temperature corresponding to C_0 on the liquidus line of the phase diagram, Fig. 2). At time $t = 0$, the temperature at $x = 0$, is lowered below the solidus temperature T_{sol}. At later times, $t > 0$, the domain $0 \leqslant x \leqslant X(t)$ is separated into distinct solid and liquid fractions, with the solid/liquid interface $x = s(t) < X(t)$ moving to the right.

In developing a model to describe the above system the following assumptions are made:

(1) Heat and mass transfer are controlled by diffusion alone. Note that in many systems the heat diffusion will be much more rapid than the mass diffusion [16] and as a result treatment of the heat diffusion can be neglected [12–14]. To maintain generality, however, in the development of the governing equations and the corresponding solution approach, diffusion of heat will be considered.

(2) The interface, $s(t)$, between the solid and the liquid is sharp and nearly planar, i.e. the smallest identifiable length scale in the mushy region is the secondary arm spacing. Previous binary alloy solutions presented by Wilson *et al.* [19, 20] have paid great attention to the assumption of a plane front. In their analysis they have shown that in some situations, although a mathematically well posed model results, the assumption of a plane front is not physically reasonable. In the context of the microsegregation problem, however, such concerns are, in general, unfounded. In essence, due to the scale of the problem, additional scale effects (e.g. surface energies associated with curvature) become important [16]. These effects, not considered by Wilson *et al.*, usually prevent

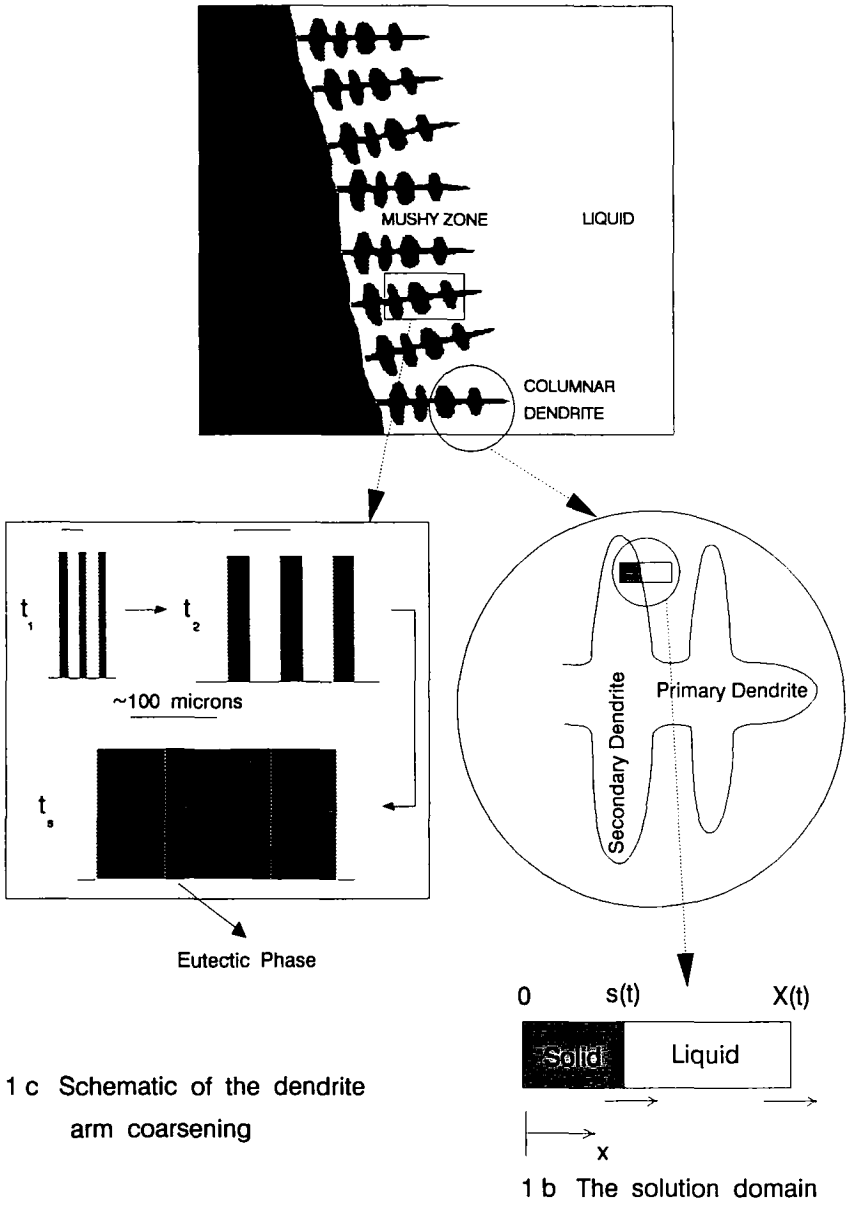

FIG. 1. Schematic of a mushy region showing dendrite arm coarsening and microsegregation solution domain.

the formation of morphologies with a smaller length scale than the secondary arms. In the systems studied in this paper, the assumption that the secondary arms are the smallest length scale, at least for the majority of the solidification, can be supported by both experimental observations, see Fig. 4.6 in ref. [16], and theoretical arguments based on a stability analysis [16, 24, 25]. This last feature will be demonstrated in Section 4.

(3) Equilibrium is maintained at the solid/liquid interface $x = s(t)$, i.e.

$$T = F_l(C_l) = F_s(C_s) \tag{1}$$

and

$$C_s = k_0 C_l \tag{2}$$

where T is temperature, continuous across the interface, C concentration, F_l and F_s the liquidus and solidus curves of the phase diagram, k_0 the equilibrium partition coefficient and the subscripts s and l stand for the solid and liquid phases, respectively.

(4) In previous binary alloy models [8–13, 15, 17–22] straight solidus and liquidus lines and a constant partition ratio are assumed. The current work, however, follows Roosz *et al.* [14] and allows for a curved solidus and liquidus, see Fig. 2, and a partition coefficient, k_0, which is dependent on the solid/liquid interface temperature.

(5) At any point in time the integrated solute content in $0 < x < X(t)$ remains at the initial composition of C_0, i.e.

$$\frac{1}{X(t)}\left[\int_0^{s(t)} \rho C_s \, dx + \int_{s(t)}^{X(t)} \rho C_l \, dx\right] = \rho_0 C_0 \tag{3}$$

where ρ is the density of the alloy.

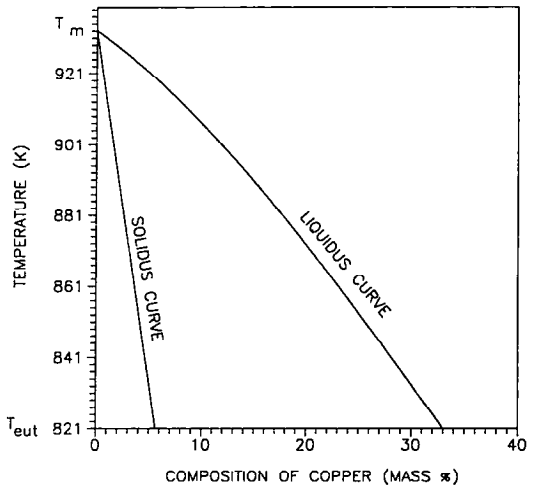

FIG. 2. Phase diagram for aluminum–copper system.

(6) To ensure mass conservation, implied in assumption 5, as the domain expands, the liquid contained in $x > X(t)$ is assumed to be at the initial concentration and liquidus temperature, i.e.

$$C = C_0 \quad \text{and} \quad T = T_{\text{liq}} \quad \text{in} \quad x > X(t).$$

(7) In terms of physical properties:

- The thermal conductivity, K, and specific heat, c, are constant within a phase but discontinuous across the phase interface.
- The liquid mass diffusivity, D_l, is constant and the solid mass diffusivity, D_s, is a function of temperature. Further, they are discontinuous across the interface.
- Compositional variations in the latent heat ΔH [26] are neglected. The density ρ is assumed to be a function of composition alone, i.e.

$$\rho = \left[\frac{100}{\frac{C}{\rho_Z} + \frac{100-C}{\rho_Y}}\right] \tag{4}$$

where ρ_Z and ρ_Y are the densities of solute Z and solvent Y.

Note that a compositionally dependent density will jump across the solidification interface. Convection effects resulting from this density difference, however, will be neglected.

(8) A key parameter in the model is the nature of the arm coarsening. In this work the arm coarsening model proposed by Roosz and co-workers [14] based on the theoretical treatment by Kattamins *et al.* [23], will be used, i.e.

$$[X(t)]^3 = 13.125 \int_0^t M \, dt \tag{5}$$

where

$$M = \frac{\gamma D_l T}{m_l(1-k_0)\Delta H C_l}$$

γ is the surface energy per unit area [J m^{-2}] and $m_l = (T_f - T_{\text{eut}})/C_{\text{eut}}$ a representative slope of the liquidus curve.

(9) Another critical feature in the model is the thermal boundary conditions. The mechanism of cooling will influence the results. In comparing with experiments it is important to match the thermal conditions to those used in the experiment. In the current work, following Battle and Pehlke [15], we will be comparing with the experiments of Sarreal and Abbaschian [27] who use a Bridgemann furnace for directional solidification experiments. In this set-up the solution domain is pulled down a prescribed temperature gradient at a pre-determined rate. This situation can be represented in the model on providing a prescribed temperature at $x = 0$.

2.3. *The two-domain governing equations*

The two-domain governing equations derived on considering the solid (s) and liquid (l) sides of $x = s(t)$ [21] are:

Heat transfer

$$\frac{\partial(\rho c_s T_s)}{\partial t} = \frac{\partial}{\partial x}\left(K_s \frac{\partial T_s}{\partial x}\right) \quad \text{in} \quad 0 \leqslant x \leqslant s(t) \tag{6}$$

$$\frac{\partial(\rho c_l T_l)}{\partial t} = \frac{\partial}{\partial x}\left(K_l \frac{\partial T_l}{\partial x}\right) \quad \text{in} \quad s(t) \leqslant x \leqslant X(t). \tag{7}$$

The temperature at $x = 0$ is prescribed (see assumption 9)

$$T(0, t) = T_0(t) = T_{\text{liq}} - \text{cooling rate} * t$$

and at the symmetry line $x = X(t)$, the domain is insulated, i.e.

$$K\frac{\partial T}{\partial x} = 0.$$

Mass transfer

$$\frac{\partial(\rho C_s)}{\partial t} = \frac{\partial}{\partial x}\left(\rho D_s \frac{\partial C_s}{\partial x}\right) \quad \text{in} \quad 0 \leqslant x \leqslant s(t) \tag{8}$$

$$\frac{\partial(\rho C_l)}{\partial t} = \frac{\partial}{\partial x}\left(\rho D_l \frac{\partial C_l}{\partial x}\right) \quad \text{in} \quad s(t) \leqslant x \leqslant X(t) \tag{9}$$

with

$$\frac{\partial C}{\partial x} = 0$$

at $x = 0$ and $X(t)$ (see assumption 5).

In the above equations the temperature, T, and concentration, C, at the solid/liquid interface $x = s(t)$, are coupled by the equilibrium constraints, equations (1) and (2). In addition, additional heat and mass

balance boundary conditions are required at $x = s(t)$ [21, 28], namely

$$\left(K_s \frac{\partial T_s}{\partial x}\right) - \left(K_l \frac{\partial T_l}{\partial x}\right) = \rho[(c_l - c_s)T_{int} + \Delta H]\frac{ds}{dt} \tag{10}$$

$$\left(\rho D_s \frac{\partial C_s}{\partial x}\right) - \left(\rho D_l \frac{\partial C_l}{\partial x}\right) = \rho(C_l - C_s)\frac{ds}{dt} \tag{11}$$

where the densities on the right-hand side of equations (10) and (11) are calculated on the solid side of the interface.

2.4. *Previous solutions*

With a fixed domain size (i.e. X = a constant) and constant density, the above equations are essentially those of the 'classical' binary alloy problem [21]. In the case of a semi-infinite domain an analytical similarity solution, due to Rubinstein [17], is available. A range of fixed domain numerical solutions have also been presented [18–22]. For example, based on an enthalpy formulation, Voller [22] uses a fixed grid 'node jumping' solution which produces results in very close agreement with the analytical solution, in particular sharp interface jumps in the concentration and enthalpy fields show no signs of numerical smearing.

Previous attempts at modeling the microsegregation problem with arm coarsening [12–14], made the additional simplifying assumptions of (1) an isothermally cooling domain (i.e. a uniform domain temperature at all times) and (2) complete solute mixing in the liquid phase. These assumptions, effectively reduce the four diffusion transport equations (equations (6)–(9)) to a single equation describing the mass diffusion in the solid phase. Heat transfer is simply dealt with on performing a transient heat balance based on prescribing a heat flux at $x = 0$ [12–14]. In these models, however, the mass balance condition, equation (11), still needs to be satisfied requiring that the front $x = s(t)$ is tracked. Ogilvy and Kirkwood use an interpolating front tracking method [29] to follow the solid/liquid front, Roosz *et al.* [14] employ a deforming space grid and time step to ensure that the front always coincides with a grid point.

Recently, Battle and Pehlke [15] have presented a microsegregation arm coarsening model based on the full governing equations (equations (6)–(11)) in which the above simplifying heat and mass transfer assumptions are not made. In this model the tracking of the front and incorporation of the heat and mass balance conditions (equations (10) and (11)) is achieved using the invariant imbedding approach [30]. The expansion of the domain is dealt with on adding in new elements at the nominal composition C_0. Although this model produces excellent agreement with a range of experiments a major drawback is the 'excessive' number of grid points, of the order of 100 000, required to maintain solute mass conservation in the expanding domain. These grid sizes result in a large computational cost (up to several days on an Apollo domain DN 4000 work station [15]). Such computation times severely limit the utility of the model.

3. A NEW MICROSEGREGATION MODEL

An objective of the microsegregation model developed in this work is to arrive at a more efficient numerical treatment of the full heat and mass transfer equations.

3.1. *Transformed equations*

Two of the major numerical difficulties in solving the governing equations (6)–(11) is in dealing with the moving boundaries, i.e.

(1) the solid/liquid interface $x = s(t) < X(t)$ at which the heat and mass balance condition, equations (10) and (11), need to be satisfied, and

(2) the right-hand boundary of the expanding domain, $x = X(t)$.

In the method proposed in this paper both of these problems are overcome on reformulation of the governing equations. The aim is to arrive at a governing formulation which can be treated with a fixed numerical space grid, i.e. one in which no special numerical features are introduced to deal with either of the moving boundaries.

The numerical problems associated with the heat and mass balance conditions are dealt with on writing the equations in a conservation form [18, 21, 22]. In the heat equation an enthalpy, H, is defined as

$$H = \rho c_s T + \delta H \tag{12}$$

where

$$\delta H = \rho f[(c_l - c_s)T + \Delta H]$$

and f is the local liquid mass fraction which has a step change from 0 to 1 at the solid/liquid interface. Note that, like the concentration C, enthalpy H is discontinuous at $x = s(t)$. In the concentration equation a variable V, the 'chemical activity' [18, 22], is defined as

$$V = \begin{cases} C_s, & x \leqslant s(t) \\ k_0 C_l, & x > s(t) \end{cases}. \tag{13}$$

Note that, like the temperature T, chemical activity V is continuous at $x = s(t)$. With these new variables single domain transport equations can be written, namely

$$\frac{\partial H}{\partial t} = \frac{\partial}{\partial x}\left(K \frac{\partial T}{\partial x}\right) \tag{14}$$

$$\frac{\partial(\rho C)}{\partial t} = \frac{\partial}{\partial x}\left(\rho D \frac{\partial V}{\partial x}\right) \tag{15}$$

where the mixture thermal conductivity is determined from

$$K = gK_l + (1-g)K_s$$

and the terms ρD and ρC are given by

$$\rho D = \rho_s(1-g)D_s + \rho_l\left(\frac{g}{k_0}\right)D_l$$

$$\rho C = \left[\rho_s(1-g) + \rho_l\left(\frac{g}{k_0}\right)\right]V$$

g represents the local liquid volume fraction (0 for fully solid to 1 for fully liquid). Equation (14) is the well-known enthalpy formulation [21]. Introduction of the variable V, has created a concentration equation, equation (15), which can be regarded as an enthalpy equation analog. In using these conservative one-domain 'enthalpy' formulations there is no need to explicitly satisfy the heat and mass balance conditions on $x = s(t)$. Other boundary conditions on the problem, however, remain the same, in particular the temperature, T, and chemical activity field, V, must still satisfy the equilibrium constraint, equation (1), at $x = s(t)$.

Solving equations (14) and (15) along with the appropriate boundary conditions would still require special treatment of the expanding domain boundary $x = X(t)$. Some authors [12, 15] adjust the size of the domain as the calculation continues on adding in additional elements at the nominal concentration, C_0, and initial temperature, T_i. Others [13, 14] keep a fixed number of elements and adjust the grid size and time step as the calculation proceeds. In this paper the problem is 'by-passed' by transforming the expanding domain $0 < x < X(t)$ into a fixed domain $0 < \xi < 1$ by means of a Landau [29, 31] transformation. On using the coordinate system

$$\xi = \frac{x}{X(t)} \tag{16}$$

and making appropriate transformations [29, 31], the partial differential equations (14) and (15) respectively become

$$\left.\frac{\partial H}{\partial t}\right|_\xi = \frac{1}{X^2}\frac{\partial}{\partial \xi}\left[K\frac{\partial T}{\partial \xi}\right] + \frac{1}{X}\frac{dX}{dt}\left[\frac{\partial(\xi H)}{\partial \xi} - H\right] \tag{17}$$

and

$$\left.\frac{\partial(\rho C)}{\partial t}\right|_\xi = \frac{1}{X^2}\frac{\partial}{\partial \xi}\left[\rho D\frac{\partial V}{\partial \xi}\right] + \frac{1}{X}\frac{dX}{dt}\left[\frac{\partial(\xi \rho C)}{\partial \xi} - \rho C\right]. \tag{18}$$

These equations are more complex than the equations in the 'real domain' (equations (14) and (15)) in that convective terms which account for domain expansion in the real space are included. A major advantage, however, is that the equations can be numerically solved on a fixed space grid using standard finite difference or finite element discretizations. In the authors' knowledge an enthalpy like formulation and the Landau transformation has not previously been used in the modeling of microsegregation.

3.2. *The numerical discretization*

The domain $0 < \xi < 1$ is subdivided into equally spaced control volumes, size $\Delta\xi$, which are arranged as shown in Fig. 3. On this grid a fully time implicit (time step Δt) central difference discretization of equations (17) and (18) is carried out resulting in the following equations:

Heat transfer

$$(\rho_P c_s + \Gamma_w^H + \Gamma_e^H)T_P = \{\rho_P^{old} c_s T_P^{old} + \Gamma_w^H T_W + \Gamma_e^H T_E + (\delta H^{old} - \delta H) - S^H\} \tag{19}$$

where

$$\Gamma_e^H = \left[\frac{K_E + K_P}{2}\right]\frac{\Delta t}{X^2(\Delta\xi)^2};$$

with a similar definition for Γ_w^H

$$\delta H_P = \rho[f_P(c_l - c_s)T_P + \Delta H]$$

and

$$S^H = \frac{\Delta t}{X}\frac{dX}{dt}\left[\frac{1}{\Delta\xi}\left(\frac{\xi_W H_W + \xi_P H_P}{2}\right) - \frac{1}{\Delta\xi}\left(\frac{\xi_P H_P + \xi_E H_E}{2}\right) + H_P\right].$$

Mass transfer

$$(\rho_P E_P + \rho_w \Gamma_w^C + \rho_e \Gamma_e^C)V_P = \{\rho_P^{old} E_P^{old} V_P^{old} + \rho_w \Gamma_w^C V_W + \rho_e \Gamma_e^C V_E - S^C\} \tag{20}$$

where

$$\Gamma_e^C = \left[\frac{D_E + D_P}{2}\right]\frac{\Delta t}{X^2(\Delta\xi)^2};$$

with a similar definition for Γ_w^C

$$\left[\rho_e = \frac{\rho_E + \rho_P}{2}\right];$$

with a similar definition for ρ_w

$$\left[\rho_P = \frac{100}{\dfrac{E_P V_P}{\rho_{Cu}} + \dfrac{(100 - E_P V_P)}{\rho_{Al}}}\right]$$

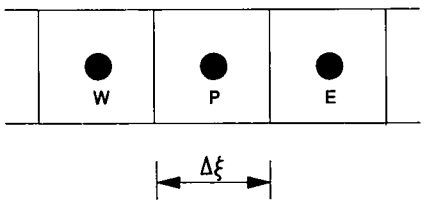

FIG. 3. Interior control volumes in the solution domain.

$$S^C = \frac{\Delta t}{X}\frac{dX}{dt}\left[\frac{1}{\Delta\xi}\left(\frac{\xi_W\rho_W C_W + \xi_P\rho_P C_P}{2}\right) - \frac{1}{\Delta\xi}\left(\frac{\xi_P\rho_P C_P + \xi_E\rho_E C_E}{2}\right) + \rho_P C_P\right]$$

and $E_P = (1-g_P)+(g_P/k_0)$. The subscripts w and e stand for west and east control volume interface while W and E stand for the west and east node points, respectively.

Note that the convective terms in equations (17) and (18) are approximated by a central difference replacement.

3.3. *Node jumping scheme*

The algorithm used to solve the above equations is the node jumping scheme proposed by Voller [22]. In this approach a fixed uniform numerical grid is used with a variable time step (which needs to be determined) such that the phase front moves from one node point to the next in each time step. It is important to recognize that at any given point in time when the solidification front is on node N, the local liquid fraction g_i is given by

$$g_i = \begin{cases} 1, & i > N \\ 0.5, & i = N \\ 0, & i < N \end{cases} \quad (21)$$

Hence with node jumping the coefficients in equations (19) and (20) can be readily evaluated. The key is to choose the required time step for any given jump. This is achieved in an iterative fashion. For illustration consider the jump from node N to $N+1$. At first the liquid fraction field is fixed at the values given by equation (21) and then the required time step is repeatedly updated until the predicted temperature and composition fields are in equilibrium at the interface, i.e.

$$T_{N+1} = F_s(V_{N+1}). \quad (22)$$

Use of a Newton update achieves convergence in 5–8 steps.

The node jumping solution procedure is executed until the liquid ahead of the solid/liquid interface reaches the eutectic composition. At this point the calculation is terminated and the current length $X(t)$ is taken as the final arm spacing. The remaining liquid in the domain is assumed to change state isothermally forming the so-called 'non-equilibrium eutectic'.

4. RESULTS AND DISCUSSION

The current model is validated with the experimental predictions for the non-equilibrium eutectic and arm spacings reported by Sarreal and Abbaschian [27]. In these experiments an aluminum 4.9 wt% copper alloy was directionally solidified at different cooling rates. The experimental cooling conditions and results are given in Table 1 and the associated physical and thermal properties are given in Table 2 [14–16]. To account for the non-linear phase diagram, see Fig. 2, the solidus and the liquidus curves are approximated on fitting piecewise linear segments of the form $F_s = a_s C_s + b_s$ and $F_l = a_l C_l + b_l$, to the data in Table 3. The interface temperature dependent partition coefficient at every point in the calculation is obtained on suitable rearrangement of these curve fits.

4.1. *Model comparisons with experiments*

In comparing the 'Landau node jumping' model with the experiments reported by Sarreal and Abbaschian [27] a fixed uniform grid of 100 control volumes was used. Table 4 compares the predicted and experimental eutectic fractions. At all but the highest cooling rate, agreement between the experimental and the numerical results is excellent. Note that, due to the decrease in time available for back diffusion, as the cooling rate increases the predicted eutectic fraction increases. At this time the authors attribute the sudden 'turn down' in the experimental results at the highest cooling rate to undercooling. The physical phenomena included in the current model will not allow for such a behavior, i.e. as the cooling rate increases the predicted eutectic will increase towards the diffusion controlled limit. This limit can be found on using a 'Scheil' assumption, i.e. simulating infinite liquid mass diffusion and no solid mass diffusion on using a relatively large value for the liquid mass diffusion (10^{-4}) and a relatively small constant value (10^{-20}) for the solid mass diffusion. The value for this limit is compared with the given predictions in Table 4. The Landau model was then implemented on making additional simplifying assumptions of constant partition coefficient ($k_0 = 0.14$) and a fixed arm spacing. This result, see column 5 in Table 4, provides an upper limit for the prediction of the eutectic. It can also be used to validate the operation of the model since under these simple assumptions the eutectic formed can also be calculated with the well-known analytical Scheil equation [16], namely

$$g^{max} = 0.8047\left(\frac{C_l}{C_0}\right)^{1/(k_0-1)} \quad (23)$$

where 0.8047 is the mass to volume conversion factor. With equation (23), the predicted $g^{max} = 8.7$ which is within 0.5% of the model prediction of 8.66.

Further insight into the role of the back diffusion in the solid can be gained on comparing the predicted solutal profile with the profile obtained when the model is run under the Scheil assumption. Figure 4 shows such a comparison, at various times, for sample 1. When solid diffusion is included in the model the transient nature of the solute profile is significant. On the other hand, if solid diffusion is removed (the Scheil assumption), the solute profile remains fixed.

In addition to predicting the eutectic formed, the proposed model can also provide an estimate of the

Table 1. Experimental conditions

Sample number	Cooling rate ($K\ s^{-1}$)	Solidification time, t_s (s)	Measured arm spacing, λ_2 (μm)	Growth rate, $G = (\lambda_2/2)/t_s$ ($\mu m\ s^{-1}$)	Measured eutectic (vol. %)†
1	0.1	980	91	0.0464	5.32
2	1.05	93.3	46	0.2465	6.23
3	11.25	8.72	23	1.3188	6.76
4	65	1.51	14	4.6358	7.09
5	187	0.52	10	9.6154	7.44
6	1700	0.058	5.4	46.5517	6.08

† Calculated from ref. [15], using equation (4).

Table 2. Physical properties of aluminum–copper alloy [14–16]

Property	Notation	Value	Units
Thermal conductivity	K_s	153	$W\ m^{-1}\ K^{-1}$
	K_l	77	
Specific heat	c_s	766	$J\ kg^{-1}\ K^{-1}$
	c_l	1179	
Latent heat	ΔH	$4.28e^5$	$J\ kg^{-1}$
Density of Al	$\rho_Y = \rho_{Al}$	2550	$kg\ m^{-3}$
Density of Cu	$\rho_Z = \rho_{Cu}$	7670	$kg\ m^{-3}$
Liquid mass diffusivity	D_l	$5e^{-9}$	$m^2\ s^{-1}$
Solid mass diffusivity	D_s	$0.29e^{-4}$ $\exp(-15610/T)$	$m^2\ s^{-1}$
Eutectic composition	C_{eut}	33.2	mass %
Eutectic temperature	T_{eut}	821.2	K
Fusion temperature	T_f	933.2	K
Liquidus temperature	T_{liq}	921.73	K
Surface energy per unit area	γ	0.093	$J\ m^2$
Gibbs–Thomson coefficient	Γ	10^{-7}	m K
Liquidus–solidus range at C_0	ΔT_0	85.73	K

Table 3. Phase diagram data [14]

T (K)	933.2	922.0	910.8	899.6	888.4	877.2	866.0	854.8	843.6	832.4	821.2
C_l (wt%)	0.0	4.8	8.9	12.3	15.5	18.8	21.8	24.8	27.5	30.2	33.0
C_s (wt%)	0.0	0.56	1.13	1.67	2.26	2.82	3.39	3.95	4.52	5.08	5.65

Table 4. Comparison of measured and predicted eutectic (in vol. %)

Sample number	Measured amount of eutectic	Predicted amount of eutectic	Diffusion controlled limit $D_s = 10^{-20}$ and $D_l = 10^{-4}$	Scheil limit $D_s = 10^{-20}$, $D_l = 10^{-4}$, $k_0 = 0.14$ and fixed arm spacing
1	5.32	5.32	7.49	8.66
2	6.23	6.25	7.49	8.66
3	6.76	6.85	7.49	8.66
4	7.09	7.11	7.49	8.66
5	7.44	7.22	7.49	8.66
6	6.08	7.36	7.49	8.66

characteristic size of the microstructure, i.e. the secondary arm spacings. Table 5 shows comparisons between the predicted and experimental arm spacings. The agreement is excellent providing additional evidence to the suitability of the general coarsening model of Roosz *et al.* [14], i.e. equation (5).

4.2. *Sensitivity analysis*

The results from the model could be sensitive to a number of the parameters and assumptions. The effects of changing various assumptions on predictions of eutectic fraction are recorded in Table 6.

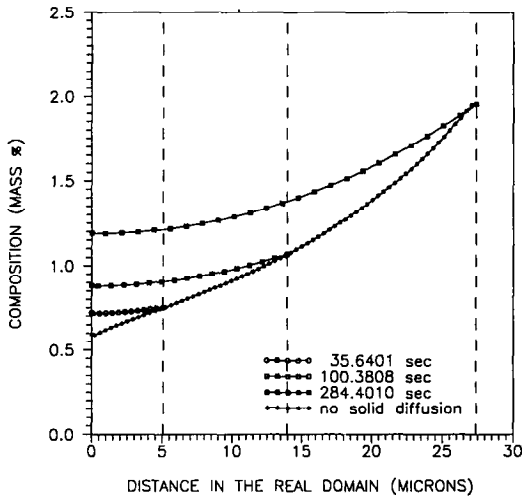

FIG. 4. Comparison of solutal profile in the solid for Sample 1 at three different times. The reference line is determined by assuming no mass diffusion in the solid ($D_s = 10^{-20}$).

Table 5. Comparison of measured and predicted arm spacing

Sample number	Measured arm spacing (μm)	Predicted arm spacing (μm)
1	91	96.5
2	46	44.1
3	23	20
4	14	11.14
5	10	7.83
6	5.4	3.75

Coarsening. If the empirically based coarsening model used by Battle and Pehlke, i.e.

$$\lambda_2 = 12.28t^{0.29} \tag{24}$$

is used in place of equation (5), very accurate arm spacing predictions are obtained but the fraction eutectic is underpredicted (see column 4 in Table 6). A good arm spacing prediction is to be expected since equation (24) essentially is an empirical fit. The underprediction of the eutectic in this case is due to the fact that equation (24) does not consider the dynamic coarsening behavior [14]. The coarsening model, i.e. equation (5), however, does include the dynamic coarsening effects. Further, if a fixed arm spacing (the experimental value) is used throughout the calculation (i.e. coarsening effects are not included) the eutectic fraction is significantly overpredicted (see column 5 in Table 6).

Cooling condition. One alternative to a prescribed temperature at $\xi = 0$ is a prescribed flux q. Column 6 in Table 6 gives the results for the case of a constant flux (chosen in each case to match the experimental solidification time). There is a significant overprediction in these results. This indicates the need to match the cooling condition used in the experiment with the one used in the model. Note that in some experiments [32] a flux condition may be reasonable.

Density. Assuming a constant density and interpreting the result as volume fraction leads to an overprediction of the volume % eutectic (see column 7 in Table 6). This illustrates the need to account for the compositional density change when solving in terms of mass fraction concentrations.

Diffusion of heat and mass. As noted in the introduction many of the previous microsegregation models [12–14] have made the assumption of infinite heat transfer in the domain and infinite liquid mass diffusion. In the context of the current experimental case such assumptions are valid. The predicted results, obtained with the model on assuming an isothermal domain cooling at a prescribed rate and infinite (large) liquid mass diffusion, are almost identical to the predictions reported in column 3 in Table 4. The current model, unlike the previous models [12–14], however, will also be valid in situations where the above assumptions cannot be made.

4.3. *Validity of the model*

The model predictions, presented above, will only be physically valid if the assumption of a near planar solid/liquid interface, i.e. the secondary dendrite arm spacing is the smallest identifiable length scale, is valid. The validity of this assumption can be shown from both experimental observation and theoretical argument.

Table 6. Sensitivity study of eutectic results

			Numerical predictions by changing one feature at a time			
			Coarsening model			
Sample number	Measured amount of eutectic	Landau node jumping model	Empirical†	Non-coarsening	With a constant flux (q) cooling	Mass density constant
1	5.32	5.32	4.73	5.90	6.87	6.44
2	6.23	6.25	5.85	7.22	7.46	7.62
3	6.76	6.85	6.45	7.98	7.86	8.38
4	7.09	7.11	6.69	8.30	8.04	8.73
5	7.44	7.22	6.77	8.40	8.11	8.88
6	6.08	7.36	6.86	8.54	8.20	9.06

†Coarsening equation (24).

Experimental observation. Metallographical examination of the final microstructure observed in the experiments by Sarreal and Abbaschian [33], showed no signs of tertiary arms, a clear indication that the secondary arm has not broken down.

Theoretical argument. In all of the results reported in this work, small constitutional undercoolings (i.e. situations in which the equilibrium temperature of the liquid ahead of the solidification interface is greater than the actual temperature) were observed. Although necessary, constitutional undercooling is not a sufficient condition for a plane front breakdown [16]. At the scale of the microsegregation problem undercoolings associated with surface tension effects will inhibit a front breakdown and the near plane front assumption will be valid. This can be demonstrated by showing that the opposing assumption that the front will breakdown is not physically reasonable. If a front breakdown were to occur, then Langer and Muller-Krumbhaar [16, 24] (using the arguments based on Mullins–Sekerka stability analysis [16, 25]) suggest that the characteristic length scale of the resulting morphology will be given by

$$R_s = 2\pi\sqrt{\left(\frac{D_l\Gamma}{G\Delta T_0}\right)} \tag{25}$$

where R_s can be viewed as the radius of curvature of a dendrite tip. Values of this characteristic length scale for the current system, calculated from the appropriate data in Tables 1 and 2, are compared with the measured secondary arm spacings in Table 7. This comparison indicates that the characteristic size of the morphology resulting from the breakdown will be of the same order, if not larger, than the characteristic size (tip radius) of the secondary arms themselves, a physically unreasonable situation. Hence, the assumption that the front breaks down leads to a physical contradiction, from which it can be concluded that the original assumption of a near plane front is valid.

4.4. *Numerical and computational considerations*

The choice of 100 grid points was determined on carrying out a grid dependence study. Table 8 reports the results of this study and clearly show that the predictions are independent of the grid size. The choice of 100 grid points is considerably less than the 100 000 reported by Battle and Pehlke [15]. These authors required this number of grid points to reduce the mass conservation errors (i.e. the difference between the nominal composition $C_0 = 4.9$ and the integrated solute composition (see assumption 5)) which were a feature of their model. The current model conserved mass for all grid densities; in fact, the mass conservation errors were always within 10^{-5}%. In the model by Battle and Pehlke [15] even at the highest grid densities, mass errors were in the range of 3%.

In terms of computational performance the currently proposed model is highly efficient. For the full model, CPU times are on the order of 2 min on a 25 MHz PC 386 with an Intel 80387 Math co-processor. In comparison, Battle and Pehlke [15] report workstation CPU times up to several days.

Table 7. Analysis of the near plane front assumption [16, 24, 25]

Sample number	Dendrite tip radius, R_s (μm)	Measured arm spacing (μm)
1	70	91
2	31	46
3	13	23
4	7	14
5	5	10
6	2.2	5.4

Table 8. Grid dependence study

Grid density	Sample number					
	1	2	3	4	5	6
25	5.55	6.12	6.83	7.12	7.23	7.38
50	5.33	6.28	6.81	7.03	7.15	7.31
100	5.32	6.25	6.85	7.11	7.22	7.36
200	5.31	6.25	6.86	7.13	7.24	7.39

5. CONCLUSIONS

The aim of this paper has been to develop a microsegregation arm coarsening model which is general in nature, provides accurate solutions on comparison with experiments, and is efficient. The proposed model, based on enthalpy like variables and utilizing the Landau transformation [29, 31] can be considered to be as general as any of the existing models [12–15]. The enthalpy variables account for the movement of the solid/liquid interface and the Landau transformation accounts for the expansion of the solution domain. Together these two approaches allow for a fixed space grid solution of the governing equations with no explicit treatment of moving boundaries. None of the previous microsegregation arm coarsening models have used enthalpy variables or a Landau transformation. The characteristic size of the microstructure and microsegregation predictions obtained with the proposed numerical model, at low and moderate cooling rates, compare well with experiments. In addition, the CPU requirement was a minute fraction of that required by the most recently proposed alternative model [15].

A brief study of the effects of the assumptions used in the model indicated that in some cases additional simplifying assumptions could be made. In particular, infinite heat transfer and infinite liquid mass transfer could be assumed with no loss of accuracy. In other cases, however, the nature of the assumptions could be critical. Examples include the coarsening and cooling mechanisms (which sould be related to the exper-

iment). A more extensive investigation of the effects of these assumptions is currently underway. Additional work will also include the investigation into the use of the proposed model as a micro component of a micro–macro model.

REFERENCES

1. W. D. Bennon and F. P. Incropera, The evolution of macro-segregation in statically cast binary ingots, *Metall. Trans. B* **18B,** 611–612 (1987).
2. C. Beckermann and R. Viskanta, Double-diffusive convection during dendritic solidification of a binary mixture, *PCH* **10,** 195–213 (1988).
3. V. R. Voller, An overview of the modeling of heat and fluid flow in solidification systems. In *Modeling of Casting, Welding and Advanced Solidification Systems.* TMS (1991).
4. J. Ni and C. Beckermann, A volume averaged two-phase model for transport phenomena during solidification, *Metall. Trans. B* **22B,** 349–361 (1991).
5. D. M. Stefanescu and C. S. Kanetkar, Modeling microstructural evolution of eutectic cast iron and of the gray/white transition, *AFS Trans.* 139–144 (1987).
6. M. Rappaz and D. M. Stefanescu, Modeling of microstructural evolution, computer applications in metal casting. In *Metals Handbook, Casting,* 9th Edn, Vol. 15, pp. 883–891 (1988).
7. M. Rappaz, Modeling of microstructure formation in solidification processes. *Int. Mater. Rev.* **34,** 93–123 (1989).
8. T. W. Clyne and W. Kurz, Solute redistribution during solidification with rapid solid state diffusion, *Metall. Trans. A* **12A,** 965–971 (1981).
9. I. Ohnaka, Mathematical analysis of solute redistribution during solidification with diffusion in solid phase, *Trans. ISIJ* **26,** 1045–1051 (1986).
10. T. Matsumiya, H. Kajioka, S. Mizoguchi, Y. Ueshima and H. Esaka, Mathematical analysis of segregations in continuously-cast slabs, *Trans. ISIJ* **24,** 873–882 (1984).
11. S. Kobayashi, Solute redistribution during solidification with diffusion in solid phase: a theoretical analysis, *J. Crystal Growth* **88,** 87–96 (1988).
12. A. J. W. Ogilvy and D. H. Kirkwood, A model for the numerical computation of microsegregation in alloys, *Appl. Scient. Res.* **44,** 43–49 (1987).
13. A Roosz, Z. Gacsi and E. G. Fuchs, Solute redistribution during solidification and homogenization of binary solid solution, *Acta Metall.* **32,** 1745–1754 (1984).
14. A. Roosz, E. Halder and H. E. Exner, Numerical calculation of micro-segregation in coarsened dendritic microstructures, *Mat. Sci. Technol.* **2,** 1149–1155 (1986).
15. T. P. Battle and R. D. Pehlke, Mathematical modeling of microsegregation in binary metallic alloys, *Metall. Trans. B* **21B,** 357–375 (1990).
16. W. Kurz and D. J. Fisher, Fundamentals of solidification, *Trans. Tech. Publs* (1986).
17. L. I. Rubinstein, *The Stefan Problem,* Translations of Mathematical Monographs, 27. American Mathematical Society (1971).
18. A. B. Crowley and J. R. Okendon, On the numerical solution of an alloy solidification problem, *Int. J. Heat Mass Transfer* **22,** 941–947 (1979).
19. D. G. Wilson, A. D. Solomon and V. Alexiades, A shortcoming of the explicit solution for the binary alloy solidification problem, *Lett. Heat Mass Transfer* **9,** 421–428 (1982).
20. D. G. Wilson, V. Alexiades and A. D. Solomon, A model of binary alloy solidification, *Int. J. Numer. Meth. Engng* **20,** 1067–1084 (1984).
21. J. Crank, *Free and Moving Boundary Problems.* Clarendon Press, Oxford (1984).
22. V. R. Voller, An implicit enthalpy solution for phase change problems with application to a binary alloy solidification, *Appl. Math. Model.* **11,** 110–116 (1987).
23. T. Z. Kattamins, J. C. Coughlin and M. C. Flemings, Influence of coarsening on dendritic arm spacing of aluminum–copper alloys, *Trans. Metall. Soc. AIME* **239,** 1504–1511 (1967).
24. J. S. Langer and H. Muller-Krumbhaar, Stability effects in dendritic crystal growth, *J. Crystal Growth* **42,** 11–14 (1977).
25. W. W. Mullins and R. F. Sekerka, Stability of a planar interface during solidification of a dilute binary alloy, *J. Appl. Phys.* **35,** 444–451 (1964).
26. D. R. Pourier and P. Nandapurkar, Enthalpies of a binary alloy during solidification, *Metall. Trans. A* **19A,** 3057–3061 (1988).
27. J. A. Sarreal and G. J. Abbaschian, The effect of solidification rate on microsegregation, *Metall. Trans. A* **17A,** 2063–2073 (1985).
28. R. B. Bird, W. E. Stewart and E. N. Lightfoot, *Transport Phenomena,* Wiley Int. Edn. Wiley, New York (1960).
29. J. Crank, Two methods for the numerical solution of moving boundary problems in diffusion and heat flow, *Q. J. Mech. Appl. Math.* **10,** 220–231 (1957).
30. G. H. Meyer, *Initial Value Methods for Boundary Value Problems.* Academic Press, New York (1973).
31. H. G. Landau, Heat conduction in a melting solid, *Q. Appl. Math.* **8,** 81–94 (1950).
32. A. B. Michael and M. B. Bever, Solidification of aluminum-rich aluminum–copper alloys, *J. Metals* 47–56 (1954).
33. G. J. Abbaschian, Private communication (November 1991).